Mode Coupling of Phonons in a Dense One-Dimensional Microfluidic Crystal

Jean-Baptiste Fleury[1]‡, **Ulf D. Schiller**[2]‡§, **Shashi Thutupalli**[3], **Gerhard Gompper**[2] **and Ralf Seemann**[1,3]

[1] Experimental Physics, Saarland University, 66123 Saarbrücken, Germany
[2] Theoretical Soft Matter and Biophysics, Institute of Complex Systems, Forschungszentrum Jülich, 52425 Jülich, Germany
[3] Max Planck Institute for Dynamics and Self-Organization, 37077 Göttingen, Germany

E-mail: `jean-baptiste.fleury@physik.uni-saarland.de`, `u.schiller@ucl.ac.uk`

Abstract. Long-living coupled transverse and longitudinal phonon modes are explored in dense, regular arrangements of flattened microfluidic droplets. The collective oscillations are driven by hydrodynamic interactions between the confined droplets and can be excited in a controlled way. Experimental results are quantitatively compared to simulation results obtained by multi-particle collision dynamics. The observed transverse modes are acoustic phonons and obey the predictions of a linearised far-field theory. The longitudinal modes arise from a non-linear mode coupling due to the lateral variation of the confined flow field. The proposed mechanism for the non-linear excitation is expected to be relevant for hydrodynamic motion in other crowded non-equilibrium systems under confinement.

Submitted to: *New J. Phys.*

‡ J.-B. F. and U. D. S. contributed equally to this work.
§ Present address: Centre for Computational Science, University College London, 20 Gordon Street, London WC1H 0AJ, United Kingdom

1. Introduction

Hydrodynamic interactions of solute objects in driven non-equilibrium systems lead to complex phenomena such as strong correlations in sedimenting suspensions [1], shock-waves in two-dimensional disordered ensembles of droplets [2], or cluster formation and alignment of red blood cells in micro-capillaries [3]. The dynamics of non-equilibrium many-body systems can be favorably studied in microfluidic systems using ordered arrangements of flowing droplets (microfluidic crystals) [4, 5]. In pioneering studies, Beatus et al. [6, 7, 8] observed collective vibrations in trains of disk like droplets flowing in a microfluidic Hele-Shaw configuration. These oscillations have been characterised as acoustic phonons with properties similar to lattice modes in dusty-plasma crystals [9]. Their dispersion relation has been obtained to linear-order in terms of a small-amplitude expansion of the ensemble flow [6, 7]. However, in contrast to solid-state phonons that can be excited in a controlled way by mechanical or optical means, microfluidic phonons have so far been observed only when excited by spontaneous asymmetries or defects in microchannels [6, 7, 8]. Possible non-linear effects and interactions between phonon modes could not be studied systematically in these settings [8, 10].

In this work, we broaden the possibility to study hydrodynamically mediated collective phenomena by exploring dense droplet systems, where spherical droplets are only slightly flattened and nearly in contact to each other. We demonstrate that long-living transverse phonon modes can be systematically excited. The controlled excited transverse phonon modes oscillate between the confining channel walls which define the preferred oscillation mode. Moreover, the non-vanishing transverse amplitude gives rise to non-linearly coupled longitudinal oscillations which are beyond the acoustic longitudinal modes observed in previous works [6, 7, 8]. The experimental measurements are confirmed by results from computer simulations using a mesoscale hydrodynamics approach which is able to reproduce the full non-linear interactions. While a linearised far-field approximation describes the transverse phonon modes of the dense droplet trains surprisingly well, the observed longitudinal modes reveal a non-linear coupling due to the influence of the confinement on the dense droplet crystal. This type of hydrodynamic coupling has impact on the self-organisation in crowded non-equilibrium systems, and is thus relevant, e.g., for controlling particle flow in applications such as microfluidic cytometry [11]. In such systems, the mild vertical confinement we explore is more realistic than the extreme confinement of Refs. [7, 8].

2. Experimental Setup and Simulation Method

Microfluidic devices to explore the collective droplet oscillations were fabricated in Sylgard 184 (Dow Corning) and bonded to glass microscopy slides using standard soft lithographic protocols [12, 13]. The flow rates were volume-controlled using computer controlled syringe pumps. Mono-disperse water droplets with radius $R \approx 64\mu$m are generated in n-hexadecane ($\rho = 773\,\text{kg/m}^3$, $\eta = 3\,\text{mPa s}$) with $2\,\text{wt}\%$ of the surfactant

Span 80 using a step-emulsification geometry [13, 14], cf. figure 1a. The spacing of the droplets in the regular trains (crystal spacing) is $a \approx 140\,\mu$m, i.e. $a < 3R$. The microchannel has uniform height and width of $H \times W \approx 120 \times 210\,\mu$m^2. The size of the droplets exceeds the height H of the microfluidic channel such that the droplets are flattened, and the drag coefficient in this case scales with R^2/H [8]. Typical flow velocities are $u_d \approx 250\,\mu$m/s for the droplet, and $u_{oil} \approx 500\,\mu$m/s for the continuous oil phase, as observed directly from microscopy images, respectively calculated from the applied volumetric flow rates. The corresponding Reynolds and Peclet number are $Re = \rho u_{\rm oil} R/\eta \approx 10^{-2}$ and $Pe = u_{\rm oil} R/D \approx 10^8$, where $D \approx 10^{-12}$cm^2/s is the diffusion coefficient of a droplet.

Computer simulations were conducted using multi-particle collision dynamics (MPC) [15, 16, 17, 18]. In this mesoscopic method, hydrodynamics are fully reproduced through the dynamics of point-like solvent particles, cf. Appendix B. The flattened droplets are modelled as discs in two-dimensional channel flow [19]. The friction with the top and bottom channel walls is included as a force $\mathbf{F}_{\rm friction} = -\gamma\mathbf{u}_{\rm d}$ where $\mathbf{u}_{\rm d}$ is the velocity of the droplet relative to the microchannel. Simulation parameters were chosen to match the experimentally observed velocity ratio $K = u_{\rm d}/u_{\rm oil}$ for an isolated droplet. The collective oscillations are modelled by an initial zigzag arrangement of droplets with a given periodicity. Droplet and flow velocities were tuned to give a Reynolds number $Re \approx 10^{-3}$ in the range of the experiments. Since MPC includes thermal fluctuations, the Peclet number $Pe \approx 10^2$ for feasible droplet and flow velocities is significantly smaller than in the experiments. This choice was dictated by a trade-off between numerical stability and computational cost. Although simulating at higher Peclet numbers is expected to reveal differences in the long term behaviour, the influence of thermal diffusion is sufficiently small to expect reliable results for short simulation times, respectively short travel distances of the droplets. Moreover, a broader range of frequencies is excited in the simulations at higher Peclet number which helps to reveal the full dispersion relation of the phonon modes as will be discussed below.

3. Controlled Excitation of Collective Oscillations

The flattened droplets experience a friction with the top and bottom channel wall and thus move slower than the surrounding liquid phase. This leads to a quasi two-dimensional dipolar flow field around each droplet, cf. figure 1b. However, note, that only the part of the dipolar field is drawn that is relevant for the effective hydrodynamic forces. The droplets produced by step emulsification self-organise into a stable zigzag configuration, where the forces from the dipolar flow fields from the neighbouring droplets cancel out [6, 13]. When this droplet arrangement is guided around a 90 degree bend, a defect in the ordering can be achieved, as displayed in figure 1c. In the resulting droplet arrangement the zigzag symmetry is broken and some droplets experience a net hydrodynamic force which drives them towards the opposite channel wall, see figure 1d.

The defect in the zigzag symmetry created in this way propagates backwards

in the co-moving frame of the droplets (see supplemental movie No. 1). If the droplet size relative to the channel width is chosen appropriately, defects can be generated periodically. The defects then initiate global sine-waves with well defined wavelength along the droplet train that travel forward in flow direction, see figure 2a and supplemental movies No. 2 and 3. The sine waves are very stable and could be observed without any change for channel lengths up to $10\,$cm, i.e. for distances more than two orders of magnitude larger than a typical wavelength. The wavelength λ along the droplet train depends on both the droplet size and the droplet spacing, i.e., droplet density. Varying these parameters, various wavelengths can be specifically excited, typically containing 4 to 9 droplets per wavelength. However, the experimentally accessible wavelength variation is limited to a factor of about three as the size of the droplets and the droplet density have to be chosen such that the droplets are close enough to affect each other by hydrodynamic interactions but do not deform each other in lateral direction by steric contact. The hydrodynamic interactions between droplets are observed to be strongly influenced by the confinement of the droplets, i.e., the degree of flattening and the absolute size of the system. The dense droplet arrangements presented in this paper could not be produced with equally sized droplets confined into channels with just $10-30\mu$m height instead of the used channel height of $120\,\mu$m, as in the shallow channels the droplets are strongly repelling each other. For an increased channel height of about 150μm at similar vertical drop confinement, we even managed to generate a collective droplet oscillation while keeping all droplets in steric contact for all times (see supplemental movie No. 4). As mentioned above, the droplet friction with the channel walls and thus the relative velocity of the droplets in the continuous phase depends on confinement ratio and linear dimension and influences the strength of the dipole forces. Numerically, we account for the different velocities by using the experimentally determined velocity ratio K.

4. Analysis of Collective Oscillations

In the following, we analyse and discuss the specific experimental and simulation results for a wavelength of six droplets with radius of $R = 64\,\mu$m and crystal spacing $a = 140\ \mu$m. The results are equally valid for other wavelengths and the discussion applies to both experiments and simulation unless mentioned otherwise. The motion of five neighbouring droplets in the co-moving frame is plotted in figure 2b,c. Due to the transverse confinement in the narrow channel and the longitudinal confinement by the crystal spacing, the space trajectory of each droplet describes a figure-eight and each droplet has a constant phase shift with respect to its neighbouring droplets. The transverse displacement has a comparably large amplitude which is given by the lateral confinement, given by the channel width W and the droplet radius R, $W-2R \approx 82\ \mu m$. This confinement defines the wavelength of the experimentally observed transverse droplet oscillation. Additionally, the flow velocity of the continuous phase across the channel is not homogeneous and slower at the channel walls as a consequence of the no

slip boundary conditions. Thus also the droplets slow down in longitudinal direction whenever the droplets closely approach the channel walls and move backward in the co-moving frame. Vice versa, the droplets travel forward in the co-moving frame when crossing the channel. The amplitude of this longitudinal oscillation is given by the crystal lattice, i.e. the droplet spacing a and the droplet radius R, $a - 2R \approx 12$ μm, which defines the stable mode in longitudinal direction and which is smaller than the amplitude in transverse direction. Thus, due to the lateral confinement, the transverse oscillation is coupled to a longitudinal oscillation where one full cycle of the longitudinal oscillation is completed while the droplet moves from one wall to the other. However, this droplet movement from one channel wall to the other only corresponds to half a transverse cycle. Accordingly, the constant phase shift between neighbouring droplets differs by a factor of two between transverse and longitudinal modes, i.e. 55° and 110° for the considered wave.

To analyse the droplet oscillations quantitatively, we recorded the droplet positions $(x_j(t), y_j(t))$ for all N droplets labelled by $j = 0 \ldots N - 1$ and for T data frames obtained every Δt. From these we extract the elongations $\delta x_j(t) = x_{j+1}(t) - x_j(t)$ and $\delta y_j(t) = y_{j+1}(t) - y_{\text{center}}$, where $x_N(t) = x_0(t) + Na$ and y_{center} is the center of the channel. The elongations were used to calculate the power spectra of the Fourier modes

$$\tilde{x}(k, \omega) = \sum_{t=0}^{T-1} \sum_{j=0}^{N-1} \delta x_j(t) \cdot \exp\left[-i\left(jka + t\omega\Delta t\right)\right] \tag{1}$$

$$\tilde{y}(k, \omega) = \sum_{t=0}^{T-1} \sum_{j=0}^{N-1} \delta y_j(t) \cdot \exp\left[-i\left(jka + t\omega\Delta t\right)\right] \tag{2}$$

for the transverse and longitudinal oscillations both from experimental and simulation results. The main feature of the experimentally observed stable mode are distinct peak values for both modes, cf. figure 3a,b. The maximum of spectral density at the main peaks indicates that the collective oscillation of the droplets is dominated by one specific wavelength. The corresponding phonon spectra obtained from simulations are displayed in figure 3c,d. They show a continuous signature revealing the full dispersion relation with a sine-like dependence of the frequency on the wave vector. This complete signature results from the small Peclet number, i.e., from the influence of thermal fluctuations that excite all the phonon modes.

A comparison of the experimental and numerical transverse power spectra shows that the dominant frequencies are identical. Moreover, they are in excellent quantitative agreement with the dispersion relation for transverse phonons $\omega_\perp(k)$ predicted by a linearized far-field theory for two-dimensional channel flow [7, 8], cf. details of the calculation Appendix C:

$$\omega_\perp(k) = 2B \sum_{j=1}^{\infty} \sin(jka) \left[1 + \cosh(j\pi\beta)\right]^2 \operatorname{csch}^3(j\pi\beta) \tag{3}$$

$$\omega_\parallel(k) = -4B \sum_{j=1}^{\infty} \sin(jka) \coth(j\pi\beta) \operatorname{csch}^2(j\pi\beta), \tag{4}$$

where $B = u_d/u_{oil}(u_{oil} - u_d)(\pi^2 R/W^2)\tan(\pi R/W)$, and $\beta = a/W$. Note that $\omega_\perp(k)$ in (3) has a slightly different form than reported in [7, 8], as it takes into account all linear-order terms in the expansion, c.f. Appendix C. The agreement of the transverse powers spectrum obtained both from experiment and simulation with the analytic dispersion relation confirms that the observed transverse oscillations are acoustic phonons. From the dispersion relation, we obtain the propagation speed $v_p \approx 312\,\mu\text{m/s}$ of the phonon mode along the droplet crystal in the direction of the flow. The dispersion relation is also in agreement with the short wavelength travelling backwards as observed experimentally for a single defect. The quantitative agreement also shows that the linearised far-field hydrodynamic interactions describe the transverse phonon dynamics remarkably well, even that the droplets nearly touch each other [8]. From the experimental findings it even seems that the validity of the far-field approximation for an ensemble of flattened and comparably large droplets is extended to smaller drop distances compared to an ensemble of micro-particles with similar confinement [4, 20].

The observed longitudinal modes are not actively excited and have a smaller amplitude compared to the transverse oscillation, but still show a clear signature especially in the simulation results. The dominant frequencies derived from experimental and simulation result agree quantitatively. Interestingly, however, the longitudinal modes show a dispersion relation that differs from the prediction of the linearised theory, cf. figure 3b,d where $\omega_\parallel(k)$ from (4) is plotted as grey lines. We observe that the maximum of the longitudinal dispersion relation appears shifted towards $k = \pi/a$, and for all k, the longitudinal modes propagate in the flow direction, in contrast to the analytical prediction (4). The observed shape of the longitudinal dispersion relation resembles the scaled shape of the transverse dispersion relation. This apparent resemblance is confirmed by the correlation strength

$$C(k_\parallel, k_\perp) = \frac{\left\langle \tilde{x}(k_\parallel, t)\tilde{y}(k_\perp, t)\right\rangle_t}{\sqrt{\left\langle |\tilde{x}(k_\parallel, t)|^2\right\rangle_t \left\langle |\tilde{y}(k_\perp, t)|^2\right\rangle_t}} \tag{5}$$

between longitudinal and transverse modes

$$\tilde{x}_\parallel(k, t) = \sum_{j=1}^N \delta x_j(t)\exp\left[-2\pi i \frac{jk}{N}\right] \tag{6}$$

$$\tilde{y}_\perp(k, t) = \sum_{j=1}^N \delta y_j(t)\exp\left[-2\pi i \frac{jk}{N}\right]. \tag{7}$$

The correlation strength is shown in figure 4a. Whereas acoustic phonons are expected to have high correlation for $k_\parallel = -k_\perp$ [10], we observe high correlation for $k_\parallel \approx +k_\perp$. For small wavelengths the dominant correlation is located around $k_\parallel = 2k_\perp$. The origin of the longitudinal modes can be explained in terms of the observed figure-eight motion of individual droplets (figure 2). The droplets slow down at both channel walls, i.e., twice during a transverse cycle such that $\omega_\parallel = 2\omega_\perp$. Spatially, a full longitudinal wave extends over each crest or trough of the transverse wave, hence $k_\parallel = 2k_\perp$. The combination leads

to the dispersion relation

$$\omega_\parallel(k) = 2\omega_\perp(k/2),$$ (8)

which is plotted in figure 3b,d and shows quantitative agreement with the observed longitudinal spectra. We conclude that the longitudinal modes do not originate from direct dipolar interactions between the droplets, but they are a consequence of the inhomogeneity of the imposed flow $\delta u(y)$ which is slower near the lateral walls. The longitudinal motion is hence coupled to the considerable amplitude of the actively excited transverse modes, because the spatial dependence of $\delta u(y)$ introduces non-linear terms in the equation of motion.

5. Long-time behaviour and onset of instability

In the numerical power spectra in figure 3c,d a weaker and apparently linear branch is present besides the main branch. The secondary branch is consistent with the faint secondary peaks in the experimental power spectra (figure 3a,b). This branch has a positive slope for transverse modes and a negative slope for longitudinal modes. In the simulation results, the linear branches are relatively weak for short simulation times, as observed experimentally but become more pronounced for longer times, which indicates a relation to the long-time behaviour of the droplets. The space-time diagram of the numerically obtained longitudinal elongations in figure 4b reveals the formation of gaps and break-up of the crystal into smaller sub-units with time. This is potentially caused by non-linear interactions between longitudinal and transverse modes, similar to observations for unconfined crystals [8] and in dusty-plasma crystals [21].

   A potential explanation for the emergence of the linear branches in the power spectra at longer times is the following: As long as the microfluidic crystal structure remains intact, the longitudinal positions of the droplets oscillate around their "equilibrium position" $x_j^{(0)}(t) = x_0(0) + ja + tu_d\Delta t$. In the co-moving frame where the first droplet oscillates around $\hat{x}_0^{(0)} = 0$ this equilibrium position is just $\hat{x}_j^{(0)} = ja$, which was already implicitly used in the Fourier transformations (1) and (2). In addition to the oscillatory motion, the droplets may diffuse away from this position over time. It may then be more appropriate to regard the droplet arrangement as a disordered ensemble, which suggests to replace the finite-differences in the equation of motion by their continuum approximations [22, 23]

$$\delta x_{n+j} - \delta x_{n-j} \approx 2ja\frac{\partial \delta x_n}{\partial x}$$ (9)

$$\delta y_{n+j} - \delta y_{n-j} \approx 2ja\frac{\partial \delta y_n}{\partial x},$$ (10)

where δx_n and δy_n are the elongations introduced above. Using this continuum approximation to derive the equations of motion and the dispersion relation as in Appendix C, we finally arrive at

$$\omega_\parallel(k) = -4\,ka\,B\sum_{j=1}^{\infty} j\,\coth(j\pi\beta)\mathrm{csch}^2(j\pi\beta)$$ (11)

$$\omega_\perp(k) = 2\,ka\,B \sum_{j=1}^{\infty} j\,[1 + \cosh(j\pi\beta)]^2 \operatorname{csch}^3(j\pi\beta). \tag{12}$$

For small ka these expressions coincide with the expansions of (3) and (4), i.e., for small ka a microfluidic crystal and a continuum show the same linearised dispersion. We note yet that the approximation in (9) and (10) demands small differences of the equilibrium positions, ja, and for the relatively strong lateral confinement between neighbouring droplets we study, hydrodynamic interactions are screened such that we can restrict the sum in the dispersion relation to the nearest neighbour interactions $j = 1$.

$$\omega_\parallel(k) = -4\,ka\,B\,\coth(\pi\beta)\operatorname{csch}^2(\pi\beta) \tag{13}$$
$$\omega_\perp(k) = 2\,ka\,B\,[1 + \cosh(\pi\beta)]^2 \operatorname{csch}^3(\pi\beta). \tag{14}$$

These dispersion relations are linear in k and are plotted as dashed lines in figure 3. They match the secondary features reasonably well. Interestingly, this also seems to be the case at the edge of the Brillouin zone, which could be a consequence of short wavelength oscillations in the subunits of the droplet train. In the simulations, these features are more pronounced because the breakup of the crystal is promoted by thermal fluctuations which may trigger instabilities leading to fast growing modes [8]. However, in our experiments, the amplitudes of the longitudinal fluctuations are not growing on the observed length and time scales, hence the secondary peaks remain faint in the experimental power spectra. This experimental observation seems to indicate that oscillations in a dense microfluidic crystal with small droplet spacing are more stable than in a microfluidic crystal with large droplet spacing [5]. A detailed stability analysis is beyond the scope of this work, however, our simulation results suggest that the considered systems of microfluidic droplets are also suited to study the nonlinear mechanisms that lead to instabilities.

6. Summary and Conclusion

Using slightly flattened droplets in a quasi two-dimensional microfluidic channel, coupled phonon modes could be experimentally studied in a dense one-dimensional microfluidic crystal and quantitatively compared to simulations and analytical results. The experimentally excited oscillation modes can be selected by the lateral droplet confinement, i.e. the droplets radius and the droplet spacing. Consequently different oscillation modes and wavelength can be controlled excited when adjusting the droplet confinement. The specifically excited transverse oscillations can be described as acoustic phonons by a linearised far-field theory even in the dense system where droplets are in steric contact. A similar behaviour could not be observed in our experiments for disk like droplets, which demonstrates that the hydrodynamic interactions are strongly influenced by the dimensionality of the system. The considerable amplitude of the excited transverse oscillations leads to a non-linear coupling of longitudinal to transverse modes. The coupling is induced by the lateral variation of the imposed flow across the

channel. The coupled longitudinal modes are beyond the existing analytic description, but can be quantitatively described by a phenomenological dispersion relation.

The small longitudinal droplet spacing in the observed dense droplet crystals supports the coupling of the longitudinal and the transverse modes leading to very stable collective oscillations. Dense and laterally confined microfluidic crystals are therefore a promising system to study collective effects and non-linear phenomena arising from hydrodynamic interactions in crowded environments out of equilibrium and under confinement. Our approach allows to gain insights into the self-organising mechanisms and can be used to improve the performance of microdroplet applications in various areas [24].

Acknowledgments

Appendix A. Particle Image Velocimetry (PIV)

Particle image velocimetry (PIV) allows to measure the flow of fluid media. The fluid is seeded with sufficiently small fluorescent tracers who follow the flow without delay. To determine the flow profile PIV does not track individual tracers but, relates on the numerical correlation of a large number of tracers whose position has been between changed between two consecutive images (double images) which have been captured within a short time interval [25, 26]. Exposure time and time delay between two consecutive images have to be adjusted to freeze the motion of the tracers and to allow for a reliable correlation of the changed tracer position. In micro-PIV, as used in our experiments, the illumination and the detection is carried out through the same microscope objective. For the experiments presented in the paper we used a commercial micro-PIV setup from LaVision (Germany) with an illumination wavelength of 473 nm and a typical time delay of 10 ms. The measured flow field is presented in Figure 1 of the paper as extracted by the commercial software DAVIS (LaVision, Germany) without further image processing.

As commercially available tracers are typically stabilised for an aqueous phase and we were interested in the flow field of the continuous phase, the PIV experiments presented in figure 1, were conducted using an oil in water emulsion. Consequently, the s table generation of monodisperse oil droplets in a surrounding water phase requires a sufficiently hydrophilic device material. Thus, the microfluidic device used for the PIV measurements has the same step geometry and channel dimensions as used for all experiments in the paper but was fabricated from the UV-curable resin NOA83H (Norland Products Inc.). The NOA83H device was molded from a PDMS master fabricated by standard soft lithography technologies. The UV curable resin was pre-

cured by an uniform UV-illumination for 10 minutes (wavelength of 365 nm and intensity of 7.5 mW/cm^2) removed from the PDMS mold and bonded to glass microscopy slides by heating the device for 10 minutes at 120°C. Prior to this step, holes were drilled in the glass slides and later connected with plastic tubing connector (Nanoport N-333. Upchurch).

Using this device monodisperse oil droplets (n-hexadecane) were generated in a surrounding aqueous phase containing 2wt% of the surfactant Sodium Dodecyl Sulfate (Sigma) and green fluorescent micro-particles (Thermo Scientific - G0100). The typical diameter of the beads is around 1 μm. A suitable concentration of tracers was achieved by diluting 0,64 ml of the original particle solution with 1,65 ml ultra pure water. Flow conditions were similar for all experiments discussed in this article.

Appendix B. Multi-particle collision dynamics

Multi-particle collision dynamics (MPC) is a mesoscopic simulation method that is capable of reproducing hydrodynamics of a solvent [15, 18]. The solvent is modelled explicitly by idealised point like particles of mass m. The fluid dynamics emerges from mass, momentum and energy transport in the particle ensemble whose equation of state is that of an ideal gas.

The particle positions and momenta are updated iteratively in successive streaming and collision steps. During the streaming step the particle moves freely

$$\mathbf{r}_i = \mathbf{r}_i + h\mathbf{v}_i, \tag{B.1}$$

where h is the time between collisions. In the collision step, the particles are sorted into cubic collision cells of size Δx. In each cell the particles then exchange momentum while the momentum of the collision cell is conserved. In this work, we use a collision rule that also conserves the angular momentum of the cell. In addition, we apply an Anderson-like thermostat to control the temperature. This collision operator is denoted as AT+a in the nomenclature of [27] and updates the particle velocities according to

$$\mathbf{v}_i^* = \mathbf{v}_C + \mathbf{v}_i^{\text{ran}} - \sum_{j \in C} \frac{\mathbf{v}_j^{\text{ran}}}{N_C} + m\Pi^{-1} \sum_{j \in C} \left[\mathbf{r}_{j,C} \times \left(\mathbf{v}_j - \mathbf{v}_j^{\text{ran}} \right) \right] \times \mathbf{r}_{i,C}, \tag{B.2}$$

where $\mathbf{v}_C$ is the centre of mass velocity of the collision cell containing N_C particles, Π is the moment of inertia tensor of the particles, $\mathbf{r}_{i,C} = \mathbf{r}_i - \mathbf{r}_C$ is the relative particle position, and $\mathbf{v}_i^{\text{ran}}$ is a random velocity drawn from a Maxwell-Boltzmann distribution. The cell grid is shifted randomly before each collision step to restore Galilean invariance of the system [28]. The dynamic viscosity η of the MPC-AT+a solvent for large number density n (particles per cell) is given by

$$\eta = \frac{nk_BTh}{\Delta x^d} \left(\frac{n}{n - (d+2)/4} - \frac{1}{2} \right) + \frac{m(n - 7/5)}{24\Delta x^{d-2}h}, \tag{B.3}$$

where k_BT is the imposed temperature and $d = 2$ is the dimensionality of the system.

The immersed droplets are modelled as rigid discs of radius R that are moved according to Newton's equation of motion. The discs are coupled to the fluid by a no-slip boundary condition. In the streaming step, a bounce-back boundary condition is applied to the solvent particles, i.e., $\mathbf{v}' = -\mathbf{v} + 2\mathbf{v}_\mathrm{b}$ where $\mathbf{v}_\mathrm{b}$ is the boundary velocity. In the collision step, the cell volume occupied by the boundary is filled with virtual particles that are distributed randomly within a layer of width $\sqrt{2}a$. The velocities of the virtual particles are drawn from a Maxwell-Boltzmann distribution and the velocity $\mathbf{v}_\mathrm{b}$ of the boundary is added [16]. The momentum change of the solvent particles during streaming and collisions is accumulated and leads to the boundary force $\mathbf{F}_\mathrm{b}$ that moves the discs [19].

Since hydrodynamics is not resolved on short distances, we add steric droplet-droplet and droplet-wall interactions. These are modelled as Weeks-Chandler-Anderson (WCA) potentials

$$V_\mathrm{WCA}(r) = 4\epsilon \left[\left(\frac{r_0}{r} \right)^{12} - \left(\frac{r_0}{r} \right)^6 \right] + \epsilon \qquad 0 < r < 2^{\frac{1}{6}} r_0, \tag{B.4}$$

where $r = r_{ij} - 2R$ for droplet-droplet interactions, and $r = r_{ij} - R$ for droplet-wall interactions. r_{ij} is the distance of the droplet centres, or the distance of the droplet centre from the wall surface, respectively.

The friction at the top and at the bottom of the Hele-Shaw cell is accounted for by a friction force $\mathbf{F}_\mathrm{friction} = -\gamma \mathbf{u}_\mathrm{d}$ where $\mathbf{u}_\mathrm{d}$ is the velocity of the droplet relative to the microchannel. The flow is driven by an external force $\mathbf{g}$ corresponding to a constant pressure gradient across the channel. The initial setup of the droplets is a triangle wave of a given wavelength λ.

The basic simulation units are chosen such that the size of an MPC collision is $\Delta x = R/5$ and the MPC time step is $h = 0.005\,\tau$, where the time scale is $\tau = (k_B T/m)^{-1/2} \Delta x$, and m is the mass of one MPC particle. The parameters for the MPC simulation are the fluid density $\rho = 40\,m/\Delta x^2$, the driving force $g = 0.1\,m\Delta x/\tau$, and the friction $\gamma = 2 \cdot 10^4\,m/\tau$. These parameters correspond to a fluid viscosity $\eta = 321.77\,m/\tau$. The mass of the droplets is given by $M = \rho \pi R^2 \approx 3140 m$. The parameters for the WCA potential are $\epsilon = k_B T$ and $r_0 = \Delta x$. We varied the channel width W, the droplet spacing a and the initial wavelength λ. The simulation results presented in the main article are for 90 droplets in a channel of length $L = 1000\Delta x$ and width $W = 15\Delta x$. The initial zigzag pattern was set up with a length of six droplets.

In order to compare the simulation results to the linearized theory and to the experiments, we determined the value $K = u_d/u_\mathrm{oil}$ from independent simulation runs with a single droplet under the same confinement. For a channel width of $W = 3R$ we obtained a value of $K \approx 0.62$ which is on the order of the experimental parameters. The oil velocity is in the range $u_\mathrm{oil} \approx 10^{-2}\Delta x/\tau$, such that the Reynolds and Peclet number of the simulations are $Re \approx 10^{-3}$ and $Pe \approx 10^2$, respectively.

Appendix C. Linearised theory and dispersion relations

The complex flow potential for a point-like dipole at position $z_j = x_j + iy_j$ in the channel evaluated at position $z = x + iy$ is [7, 8]

$$
\begin{aligned}
w_j(z) &= \frac{\pi R^2 \delta u_0}{2W} \left\{ \coth\left[\frac{\pi(z - z_j - iy_j)}{2W} \right] \right. \\
&\quad + \left. \coth\left[\frac{\pi(z - z_j - i(W - y_j))}{2W} \right] \right\} \\
&= \frac{\pi R^2 \delta u_0}{2W} \left\{ \coth\left[\frac{\pi(x - x_j + i(y - 2y_j))}{2W} \right] \right. \\
&\quad + \left. \coth\left[\frac{\pi(x - x_j + i(y - W))}{2W} \right] \right\}.
\end{aligned}
\tag{C.1}
$$

Differentiating $w_j(z)$ with respect to z we obtain

$$
\begin{aligned}
\frac{dw_j}{dz} &= -\frac{\pi^2 R^2 \delta u_0}{4W^2} \left\{ \operatorname{csch}^2\left[\frac{\pi(z - z_j - iy_j)}{2W} \right] \right. \\
&\quad + \left. \operatorname{csch}^2\left[\frac{\pi(z - z_j - i(W - y_j))}{2W} \right] \right\} \\
&= -\frac{\pi^2 R^2 \delta u_0}{4W^2} \left\{ \operatorname{csch}^2\left[\frac{\pi(x - x_j + i(y - 2y_j))}{2W} \right] \right. \\
&\quad + \left. \operatorname{csch}^2\left[\frac{\pi(x - x_j + i(y - W))}{2W} \right] \right\}.
\end{aligned}
\tag{C.2}
$$

Note that dw_j/dz is related to the force exerted on other droplets, and it does not contain terms involving the velocity $\dot{x}_j$ or $\dot{y}_j$ of the droplets.

We expand around $x_n = na$, $x_{n+j} = (n + j)a$, $y_n = 0$, and $y_{n+j} = 0$ and keep all linear terms

$$
\begin{aligned}
\frac{dw_j}{dz} &\approx -\frac{\pi^2 R^2 \delta u_0}{4W^2} \left\{ 4\operatorname{csch}^2\left(\frac{aj\pi}{W} \right) \right. \\
&\quad - \frac{4\pi i}{W}\operatorname{csch}^3\left(\frac{aj\pi}{W} \right) \left[1 + \cosh\left(\frac{aj\pi}{W} \right) \right]^2 \delta y_{n+j} \\
&\quad + \frac{8\pi i}{W} \coth\left(\frac{aj\pi}{W} \right) \operatorname{csch}^2\left(\frac{aj\pi}{W} \right) \delta y_n \\
&\quad + \left. \frac{8\pi}{W} \coth\left(\frac{aj\pi}{W} \right) \operatorname{csch}^2\left(\frac{aj\pi}{W} \right) (\delta x_n - \delta x_{n+j}) \right\}
\end{aligned}
\tag{C.3}
$$

Now we add the expansion of dw_{-j}/dz around $x_{n-j} = (n - j)a$ and arrive at

$$
\begin{aligned}
\frac{dw_j}{dz} + \frac{dw_{-j}}{dz} &\approx -\frac{\pi^2 R^2 \delta u_0}{4W^2} \left\{ 8\operatorname{csch}^2\left(\frac{aj\pi}{W} \right) \right. \\
&\quad - \frac{4\pi i}{W}\operatorname{csch}^3\left(\frac{aj\pi}{W} \right) \left[1 + \cosh\left(\frac{aj\pi}{W} \right) \right]^2 (\delta y_{n+j} - \delta y_{n-j}) \\
&\quad - \left. \frac{8\pi}{W} \coth\left(\frac{aj\pi}{W} \right) \operatorname{csch}^2\left(\frac{aj\pi}{W} \right) (\delta x_{n+j} - \delta x_{n-j}) \right\}.
\end{aligned}
\tag{C.4}
$$

Since the expansion of the compressibility factor C around $y_j = 0$ has a vanishing linear term, we can readily multiply with $C = \frac{W}{\pi R} \tan\left(\frac{\pi R}{W}\right)$ and K, and sum over j to obtain the equations of motion for the nth droplet

$$\dot{\delta x_n} = 2K\delta u_0 \frac{\pi^2 R}{W^2} \tan\left(\frac{\pi R}{W}\right)$$

$$\cdot \sum_{j=1}^{\infty} \coth\left(\frac{aj\pi}{W}\right) \operatorname{csch}^2\left(\frac{aj\pi}{W}\right) (\delta x_{n+j} - \delta x_{n-j}) \tag{C.5}$$

$$\dot{\delta y_n} = -K\delta u_0 \frac{\pi^2 R}{W^2} \tan\left(\frac{\pi R}{W}\right)$$

$$\cdot \sum_{j=1}^{\infty} \operatorname{csch}^3\left(\frac{aj\pi}{W}\right) \left[1 + \cosh\left(\frac{aj\pi}{W}\right)\right]^2 (\delta y_{n+j} - \delta y_{n-j}). \tag{C.6}$$

Plugging in a plane wave solution we arrive at the dispersion relations

$$\omega_\parallel(k) = -4B \sum_{j=1}^{\infty} \sin(jka) \coth(j\pi\beta) \operatorname{csch}^2(j\pi\beta) \tag{C.7}$$

$$\omega_\perp(k) = 2B \sum_{j=1}^{\infty} \sin(jka) \left[1 + \cosh(j\pi\beta)\right]^2 \operatorname{csch}^3(j\pi\beta), \tag{C.8}$$

where we introduced the prefactors $B = c_0(\pi^2 R/W^2) \tan(\pi R/W)$, $c_0 = K(u_{\text{oil}} - u_d)$, $\beta = a/W$, and $K = u_d/u_{\text{oil}}$ as in [7, 8].

References

[1] Sriram Ramaswamy. Issues in the statistical mechanics of steady sedimentation. *Adv. Phys.*, 50(3):297–341, May 2001.

[2] Tsevi Beatus, Tsvi Tlusty, and Roy Bar-Ziv. Burgers shock waves and sound in a 2d microfluidic droplets ensemble. *Phys. Rev. Lett.*, 103(11):114502–, September 2009.

[3] J. Liam McWhirter, Hiroshi Noguchi, and Gerhard Gompper. Flow-induced clustering and alignment of vesicles and red blood cells in microcapillaries. *Proc. Natl. Acad. Sci.*, 106(15):6039–6043, April 2009.

[4] M. Baron, J. Bawzdziewicz, and E. Wajnryb. Hydrodynamic crystals: Collective dynamics of regular arrays of spherical particles in a parallel-wall channel. *Phys. Rev. Lett.*, 100(17):174502, April 2008.

[5] N. Desreumaux, N. Florent, E. Lauga, and D. Bartolo. Active and driven hydrodynamic crystals. *Eur. Phys. J. E*, 35(8):1–11, 2012.

[6] Tsevi Beatus, Tsvi Tlusty, and Roy Bar-Ziv. Phonons in a one-dimensional microfluidic crystal. *Nature Phys.*, 2(11):743–748, November 2006.

[7] Tsevi Beatus, Roy Bar-Ziv, and Tsvi Tlusty. Anomalous microfluidic phonons induced by the interplay of hydrodynamic screening and incompressibility. *Phys. Rev. Lett.*, 99(12):124502, September 2007.

[8] Tsevi Beatus, Roy Bar-Ziv, and Tsvi Tlusty. The physics of 2d microfluidic droplet ensembles. *Phys. Rep.*, 516(3):103–145, July 2012.

[9] S. V. Vladimirov, P. V. Shevchenko, and N. F. Cramer. Vibrational modes in the dust-plasma crystal. *Phys. Rev. E*, 56(1):R74–R76, July 1997.

[10] Bin Liu, J. Goree, and Yan Feng. Waves and instability in a one-dimensional microfluidic array. *Phys. Rev. E*, 86(4):046309, October 2012.

[11] Xiaole Mao, Sz-Chin Steven Lin, Cheng Dong, and Tony Jun Huang. Single-layer planar on-chip flow cytometer using microfluidic drifting based three-dimensional (3d) hydrodynamic focusing. *Lab Chip*, 9:1583–1589, 2009.

[12] David C. Duffy, J. Cooper McDonald, Olivier J. A. Schueller, and George M. Whitesides. Rapid prototyping of microfluidic systems in poly(dimethylsiloxane). *Anal. Chem.*, 70(23):4974–4984, October 1998.

[13] Venkatachalam Chokkalingam, Stephan Herminghaus, and Ralf Seemann. Self-synchronizing pairwise production of monodisperse droplets by microfluidic step emulsification. *Appl. Phys. Lett.*, 93(25):254101–3, December 2008.

[14] Craig Priest, Stephan Herminghaus, and Ralf Seemann. Generation of monodisperse gel emulsions in a microfluidic device. *Appl. Phys. Lett.*, 88(2):024106–3, January 2006.

[15] Anatoly Malevanets and Raymond Kapral. Mesoscopic model for solvent dynamics. *J. Chem. Phys.*, 110(17):8605–8613, May 1999.

[16] Ingo O. Götze, Hiroshi Noguchi, and Gerhard Gompper. Relevance of angular momentum conservation in mesoscale hydrodynamics simulations. *Phys. Rev. E*, 76(4):046705, October 2007.

[17] Raymond Kapral. Multiparticle collision dynamics: Simulation of complex systems on mesoscales. *Adv. Chem. Phys.*, 140:89, 2008.

[18] G. Gompper, T. Ihle, D. M. Kroll, and R. G. Winkler. Multi-particle collision dynamics: A particle-based mesoscale simulation approach to the hydrodynamics of complex fluids. *Adv. Poly. Sci.*, 221:1–87, 2009.

[19] Ingo O. Götze and Gerhard Gompper. Dynamic self-assembly and directed flow of rotating colloids in microchannels. *Phys. Rev. E*, 84:031404, Sep 2011.

[20] Bianxiao Cui, Haim Diamant, and Binhua Lin. Screened hydrodynamic interaction in a narrow channel. *Phys. Rev. Lett.*, 89(18):188302, October 2002.

[21] Bin Liu, J. Goree, and Yan Feng. Mode coupling for phonons in a single-layer dusty plasma crystal. *Phys. Rev. Lett.*, 105(8):085004, August 2010.

[22] Philip Rosenau. Dynamics of nonlinear mass-spring chains near the continuum limit. *Phys. Lett. A*, 118(5):222–227, October 1986.

[23] Jonathan A. D. Wattis. Quasi-continuum approximations to lattice equations arising from the discrete nonlinear telegraph equation. *J. Phys. A*, 33(33):5925, 2000.

[24] Ashleig B. Theberge, Fabienne Courtois, Yolanda Schaerli, Martin Fischlechner, Chris Abell, Florian Hollfelder, and Wilhelm T. S. Huck. Microdroplets in microfluidics: An evolving platform for discoveries in chemistry and biology. *Angew. Chem. Int. Ed.*, 49(34):5846–5868, 2010.

[25] Ralph Lindken, Lichuan Gui, and Wolfgang Merzkirch. Velocity measurements in multiphase flow by means of particle image velocimetry. *Chem. Eng. Tech.*, 22(3):202–206, 1999.

[26] Ralph Lindken, Massimiliano Rossi, Sebastian Große, and Jerry Westerweel. Micro-particle image velocimetry (μpiv): Recent developments, applications, and guidelines. *Lab Chip*, 9(17):2551–2567, 2009.

[27] Hiroshi Noguchi and Gerhard Gompper. Transport coefficients of off-lattice mesoscale-hydrodynamics simulation techniques. *Phys. Rev. E*, 78(1):016706, July 2008.

[28] T. Ihle and D. M. Kroll. Stochastic rotation dynamics: A Galilean-invariant mesoscopic model for fluid flow. *Phys. Rev. E*, 63(2):020201, January 2001.
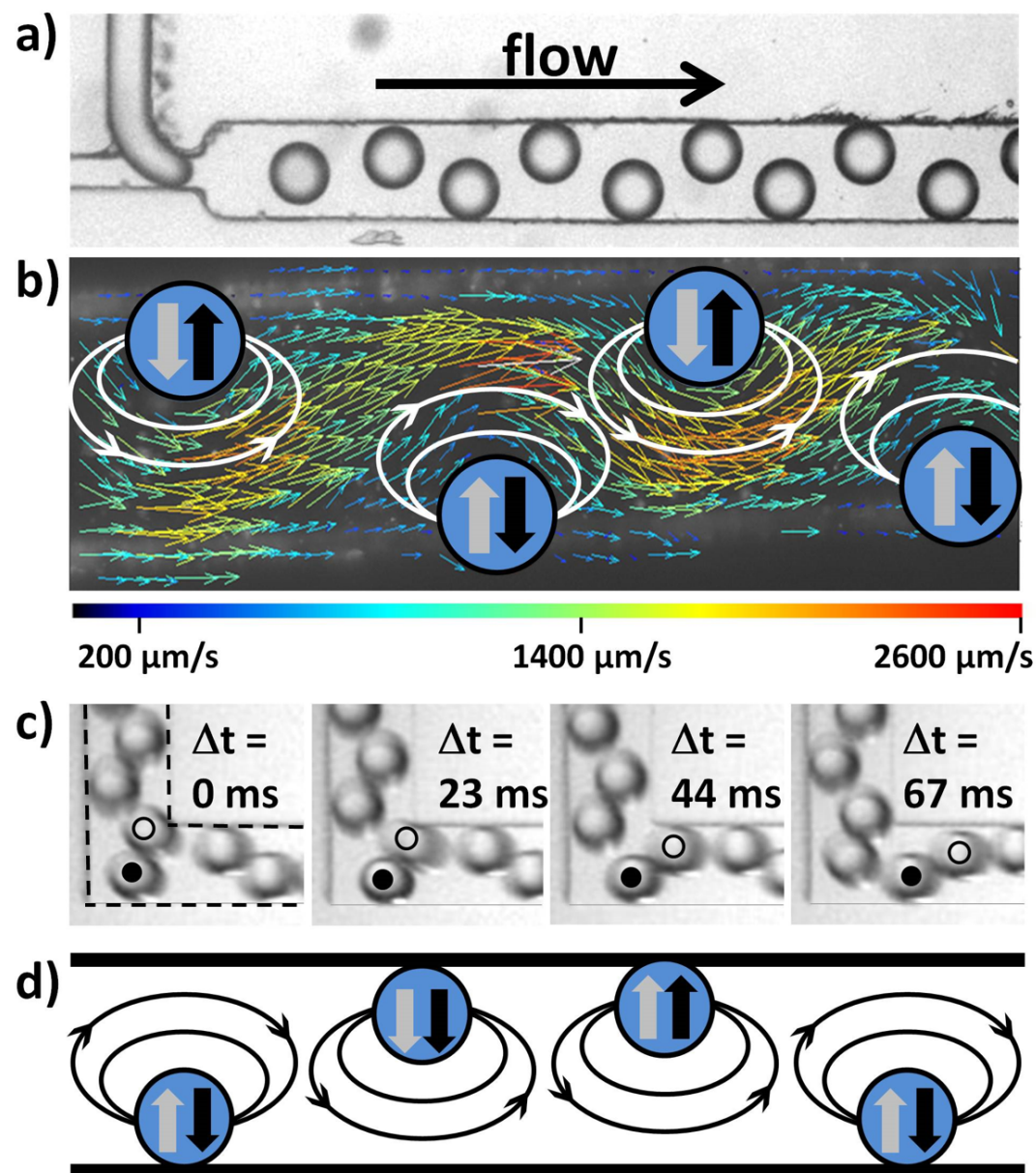
Figure 1. a) Generation of microfluidic crystals using a step-emulsification geometry. b) Flow field determined by particle image velocimetry in the lab frame. Note, that for experimental reasons a different device material and emulsion system had to be used for the PIV-experiments as explained in Appendix A. The relevant dipolar flow fields around each droplet in the co-moving frame of the droplets are sketched by white arrows. The second half of the dipolar flow field close to the channel wall is omitted for the sake of clarity. The transverse forces resulting from the dipolar flow fields from leading and trailing droplets are shown as grey and black arrows, respectively. c) Microscopy time series showing the droplet reorganization at a 90° bend. The boundaries of the bend were indicated in the first image. The droplet marked with a dot is repelled from the corner due to its hydrodynamic image [7, 8] and the trailing droplet marked with a circle is squeezed between the leading droplet and the wall and propelled longitudinally out of the corner. d) Sketch indicating the dipolar flow fields and the resulting transverse forces in a zigzag arrangement with one defect. The width of the main channel is $W = 210\,\mu$m for tiles a)-c).
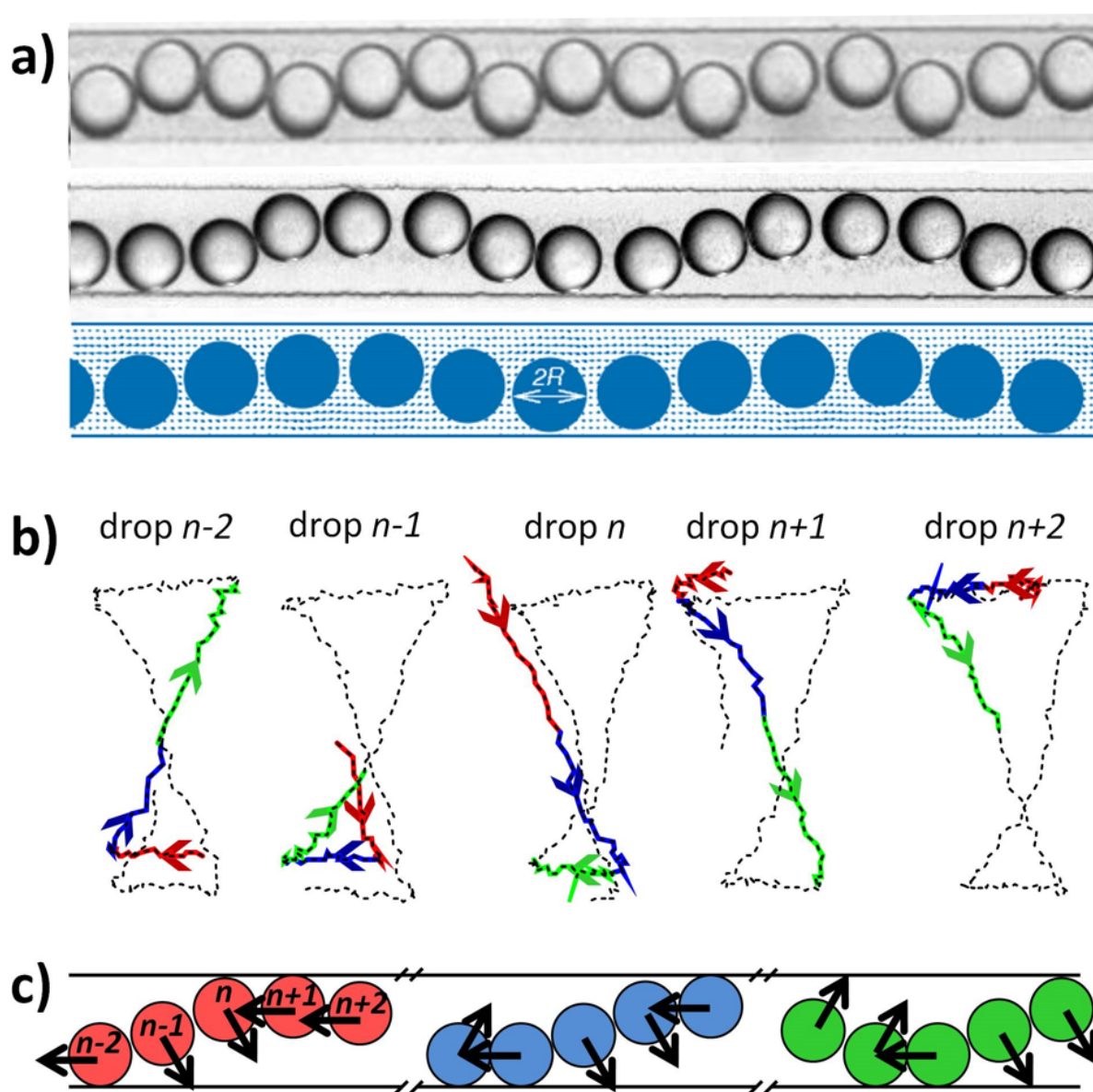
Figure 2. a) Travelling sine waves with different wavelength as generated by periodic defects for two different droplet sizes (*top*) and by numerical simulation (*bottom*). The width of all microfluidic channels are $W = 210 \, \mu$m. b) Configuration space trajectory of five neighbouring droplets in the co-moving frame of the droplets as extracted from the experiments. To avoid overlaps, the lateral distance between the trajectories was increased. The trajectories of three time intervals are coloured in red (light grey), blue (dark grey), and green (grey). c) Sketch of the five droplets from b) using the same colour code with indicated directions of motion in the co-moving frame of the droplets.
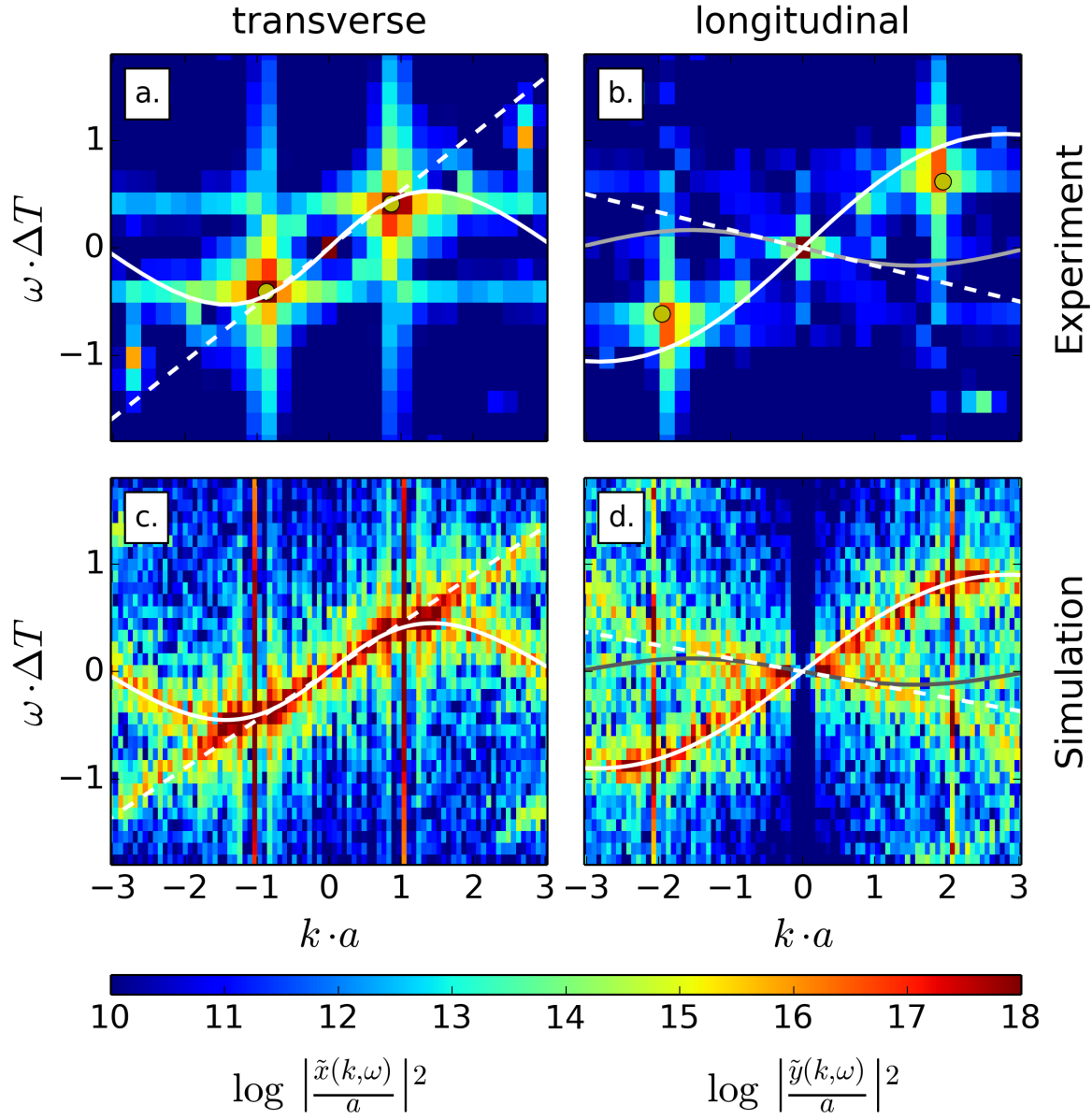
Figure 3. Power spectra of the Fourier transform of the droplet oscillations as extracted from experimental a,b) and simulation results c,d). a,c) Transverse modes $y(k,\omega)$; the white solid curves denote the prediction for acoustic phonons from the linearised theory (3) for $\omega_\perp(k)$ whereas the white dashed lines correspond to the continuum approximation with nearest neighbour interactions only. b,d) Longitudinal modes $x(k,\omega)$. The black/grey solid curves are the prediction $\omega_\parallel(k)$ from (4) whereas the dashed lines correspond to the continuum approximation. The white solid curves represent $2\omega_\perp(k/2)$ and illustrate the coupling of the longitudinal to the transverse modes. The circle symbols mark the main peaks of the experimental spectrum indicating the preferred wave vectors. The time scale is $\Delta T = R/u_d$.
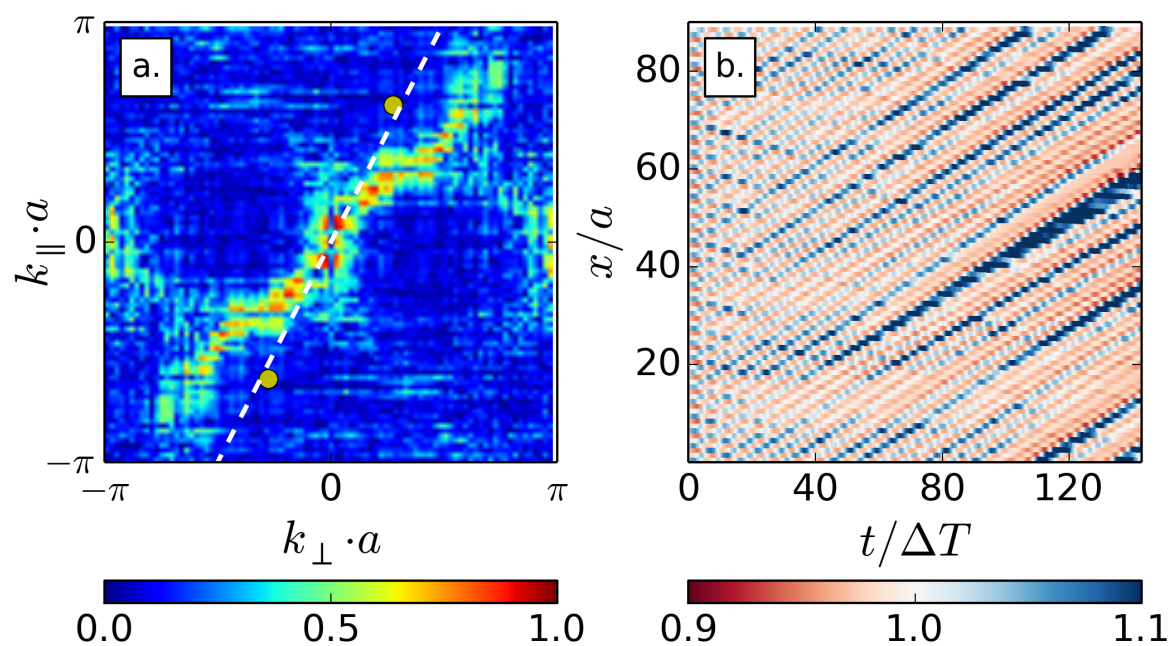
Figure 4. a) Correlation strength $C(k_\parallel, k_\perp)$ of longitudinal and transverse phonons as determined from the numerical simulation. The circle symbols mark the dominating wave vectors observed experimentally (extracted from Fig. 3. The dashed line represents the phenomonelogical dispersion relation $k_\parallel = 2k_\perp$ discussed in the text. b) Space-time diagram of the longitudinal droplet distance observed in simulation results.